Earth, Planets and Space

FULL PAPER

Open Access

O^+ density distribution in the nightside ionosphere reconstructed from ISS-IMAP/EUVI data

Shin'ya Nakano[1,2,3*], Yuta Hozumi[4,5,6], Akinori Saito[7], Ichiro Yoshikawa[8], Atsushi Yamazaki[9], Kazuo Yoshioka[8] and Go Murakami[9]

Abstract

The O^+ density distribution in the nightside ionosphere has been reconstructed from extreme ultraviolet (EUV) images taken by the EUVI-B imager of the International Space Station Ionosphere, Mesosphere, upper Atmosphere, and Plasmasphere mapping (ISS-IMAP) cameras. The EUVI-B imager covers the wavelength range from about 70 nm to 110 nm and mainly observes the 91.1 nm emission from the recombination of O^+ ions and electrons. Assuming that the electron density is equal to the O^+ density in the *F*-region where the imager observes, the EUV intensity observed by EUVI-B is approximately proportional to the line-of-sight integral of the square of the O^+ density. This enables us to estimate the O^+ density distribution in the *F*-region from a sequence of EUVI-B data in each International Space Station (ISS) orbit with a Bayesian method. We demonstrate the reconstruction of the O^+ distribution. In particular, the O^+ density structure of the equatorial ionization anomaly (EIA) in the vicinity of an ISS orbit is obtained.

Keywords O^+ ion distribution, Ionosphere, Extreme ultraviolet measurement

Graphical Abstract

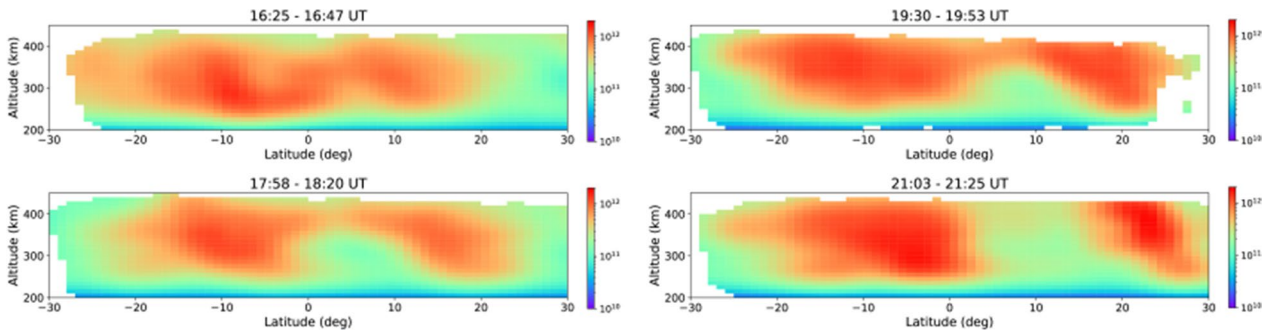

*Correspondence:
Shin'ya Nakano
shiny@ism.ac.jp
Full list of author information is available at the end of the article

Introduction

The International Space Station Ionosphere, Mesosphere, Atmosphere, and Plasmasphere mapping (ISS-IMAP) mission operates a suite of imagers on board the International Space Station (ISS). One of the imagers, EUVI-B, covers the wavelength range from about 70 nm to 110 nm (Yoshikawa et al. 2011; Uji et al. 2014). This imager was intended to observe extreme ultraviolet (EUV) emissions at 83.4 nm scattered by O^+ ions. However, our previous study (Nakano et al. 2021) concluded that EUVI-B mostly observes the 91.1 nm emission due to recombination between O^+ ions and electrons during nighttime. The ISS orbits at about 400 km and the EUVI-B imager was oriented to observe the *F*-region of the ionosphere. In the *F*-region, the electron density is approximately equal to the O^+ density. We can thus assume that the EUV intensity observed from EUVI-B is approximately proportional to the line-of-sight integral of the square of the O^+ density. This motivated us to use the EUVI-B data for tomographic reconstruction of the O^+ density distribution around the ISS orbit in the nightside ionosphere.

Dymond et al. (2017a, b) also reconstructed the O^+ density distribution with 91.1 nm EUV images observed by the Special Sensor Ultraviolet Limb Imager (SSULI) instruments on board the Defense Meteorological Satellite Program (DMSP) Block 5D3 satellites. While the DMSP satellites orbit at about 800 km altitude, the ISS orbits at about 400 km, which is close to the *F*-region. This orbital altitude potentially allows us to resolve a more detailed structure of the *F*-region with a high-resolution imager. This study aimed to demonstrate the reconstruction of O^+ density distribution from the EUVI-B data of ISS-IMAP. The EUVI-B imager normally took EUV images with a time interval of 102 seconds. The sequence of the images acquired in each ISS orbit was utilized to obtain the three-dimensional O^+ distribution (latitude, longitude, and altitude) in the vicinity of the orbit, although the present paper reports the latitudinal and altitudinal structures. Since reconstruction results can be obtained every ISS orbit, with a period of about 90 min, we could obtain the temporal evolution of the ionospheric structure with a temporal resolution of about 90 min. Since the ISS orbits at low and mid latitudes, variations of the equatorial ionization anomaly (EIA) (e.g., Appleton 1946) can be analyzed.

Data

The ISS-IMAP telescopes on board the ISS conducted limb observations of the Earth's ionosphere. The ISS orbits at about 400 km altitude, and its orbital inclination is 51°. The ISS-IMAP imagers were directed toward the aft direction of the ISS orbit. The EUVI-B imager took EUV images with an exposure time of 60 seconds and normally with an observation cadence of 102 seconds. The nominal field of view of EUVI-B is $13.2° \times 13.2°$. Each image taken from EUVI-B contains 128×128 pixels. However, some of the pixels cannot be used for scientific purposes. Figure 1 shows statistics of all the pixels for the period from 10 December 2012 to 1 January 2013. The left panel shows the average of the detected count per min for each pixel and the right panel shows the standard deviation of the count per min. In the corners, the average and standard deviation are near zero. The substantial field of view is thus the circular area in the square image. The figure shows that the pixels in the rim of the field of view do not correctly detect the EUV flux. Moreover, some parts in the right half of the images showed abnormal values probably because the sensors were damaged. We exclude these noisy pixels, and only

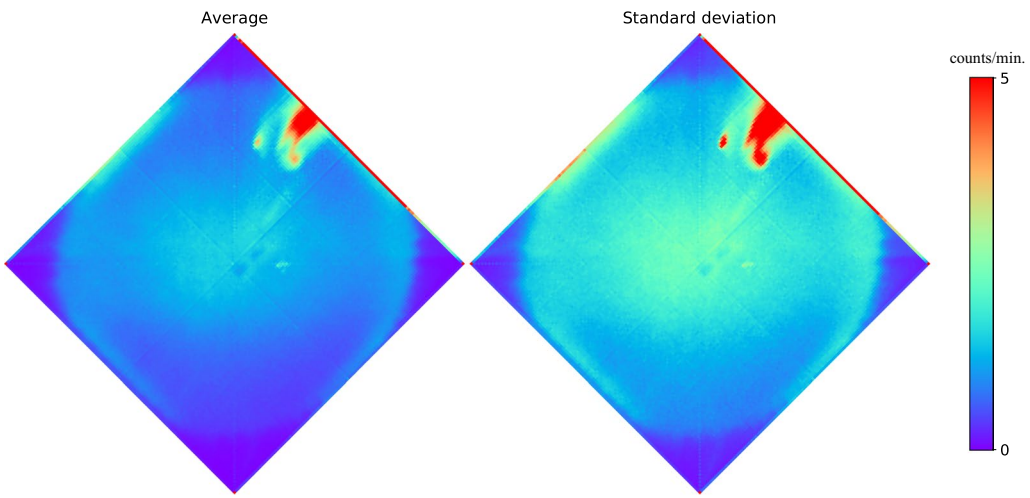

Fig. 1 Average (left) and standard deviation (right) for the data from 10 December 2012 to 1 January 2013

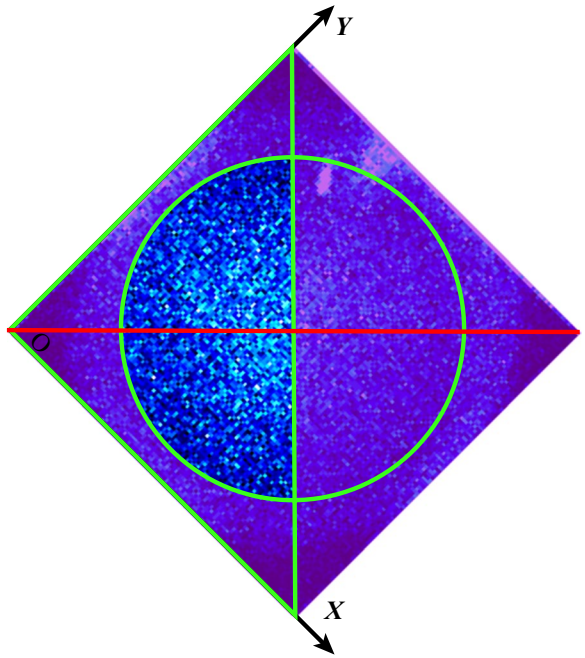

Fig. 2 Region of each image used for observations. The purple-shaded area is excluded

use the data from the pixels within the region indicated in Figure 2, which is defined as

$$X_j + Y_j < 128, \tag{1a}$$

$$\sqrt{(X_j - C_X)^2 + (Y_j - C_Y)^2} < 56, \tag{1b}$$

where X_j and X_j are the X and Y coordinates of the jth pixel on an image and (C_X, C_Y) indicates the center of the image. Equation (1a) excludes the upper-right half of each image where many of the EUV detectors were damaged. Equation (1b) excludes the noise in the rim of each image.

Figure 1 also indicates that the observed signal tended to be stronger around the center of an image than in areas away from the center. Figure 3 shows the statistics in Figure 1 along the horizontal line indicated with a red line in Figure 2. The left panel shows the average of the data from 10 December 2012 to 1 January 2013 along this line, the middle panel the standard deviation, and the right panel the square root of the difference between the variance and average. In each panel, the region excluded by the criteria in Eqs. (1a) and (1b) is shaded with gray. If the sensitivity was uniform over all the pixels, the average EUV flux along the horizontal line would be flat because the horizontal structure of the ionosphere would be approximately uniform on average. However, the average flux was larger in the center than off-center. The standard deviation was also larger in the center. This indicates high sensitivity around the center of the imager. We estimate the sensitivity from $\sqrt{\sigma_{y_j}^2 - \bar{y}_j}$ where $\bar{y}_j$ and $\sigma_{y_j}^2$ denote the mean and variance of the observed signal for jth pixel as discussed in Appendix. The shape of s_j was determined so that it well matches the profile of $\sqrt{\sigma_{y_j}^2 - \bar{y}_j}$ in the bottom panel of Figure 3. We assume a sensitivity for the jth pixel as

$$s_j = 0.0018 \times \left(\frac{4}{9} \exp\left[-\frac{(X_j - C_X)^2 + (Y_j - C_Y)^2}{28} \right]^2 + \frac{5}{9} \right), \tag{2}$$

where 0.0018 [counts/s/Rayleigh/bin] is the sensitivity determined based on ground calibrations for 91.1 nm EUV (Uji et al. 2014; see also Page 5 of our previous paper Nakano et al. 2021). Equation (2) thus assumes that the peak sensitivity approximately matches the experimental value. The red line in the lower panel of Figure 3 shows the curve of s_j in Eq. (2) after adjusting the vertical scale.

Method of estimation

91.1 nm EUV

This study assumes that the EUV flux observed by the EUVI-B imager is attributed to 91.1 nm emission due to the recombination of O^+ ions and electrons. Although EUVI-B can also detect 98.9 nm and 102.6 nm emissions, the contributions of these emissions are estimated to be minor (Nakano et al. 2021). Therefore, we only consider 91.1 nm EUV in this study. The 91.1-nm EUV flux due to the O^+ recombination F_r is obtained by the following integral along line of sight:

$$F_r = \frac{1}{4\pi} \int_0^\infty \kappa e^{-\tau} n_e n_{O^+} \, d\ell, \tag{3}$$

where n_e is the electron density and n_{O^+} the O^+ ion density. The radiative recombination coefficient κ is set to be $\kappa = 3.5 \times 10^{23} \times (1160/T)\mathrm{m}^3/\mathrm{s}$ (Meléndez-Alvira et al. 1999), where T is the electron temperature in Kelvin and it is given by the International Reference Ionosphere (IRI) model (Bilitza et al. 2014) in this study. The optical depth τ is given by the following line-of-sight integral:

$$\tau = \sum_m \int_0^\ell \alpha_m n_m(\boldsymbol{r}(s)) \, ds, \tag{4}$$

where m denotes the absorbing species, α_m is the absorbing cross-section for the species, and n_m is the number density for the species. We take into account the absorption due to N_2, O, and O_2. The absorption coefficients for 91.1 nm EUV are set to be $14.5 \times 10^{-22}\,\mathrm{m}^2$, $3.93 \times 10^{-22}\,\mathrm{m}^2$, and $15.34 \times 10^{-22}\,\mathrm{m}^2$ for N_2, O, and O_2, respectively, according to Dymond et al. (2017b). The

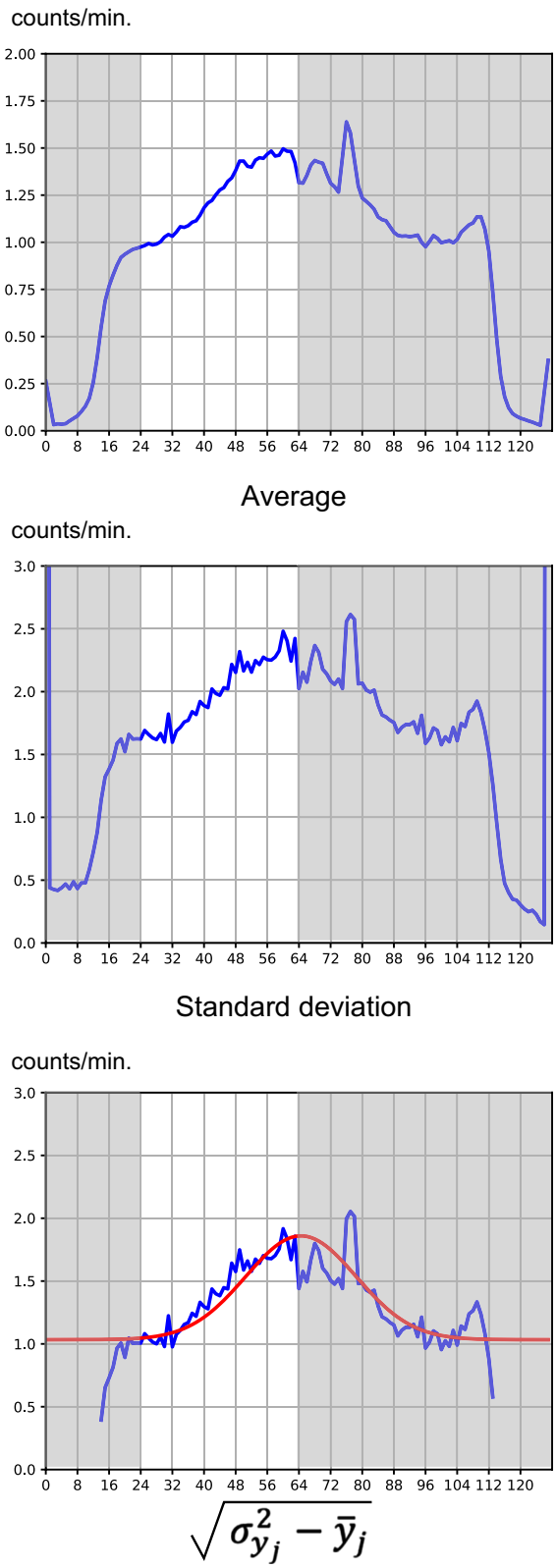

Fig. 3 Profile along the red horizontal line in **Figure 2** of the average (upper), standard deviation (middle), and square root of the difference between the variance and average (lower) for the data from 10 December 2012 to 1 January 2013 shown in **Figure 1**. The red line in the lower panel indicates the curve in Eq. (2) after adjusting the vertical scale

number densities for the absorbing species are assumed based on the Naval Research Laboratory Mass Spectrometer and Incoherent Scatter Radar Exosphere (NRLMSISE-00) model (Picone et al. 2002). Assuming that the electron density is approximately equal to the O^+ density in the *F*-region, Eq. (3) can be approximated as

$$F_r \approx \frac{1}{4\pi} \int \kappa e^{-\tau(\boldsymbol{r})} [n_{O^+}(\boldsymbol{r})]^2 \, d\ell. \tag{5}$$

This equation shows that only the O^+ density n_{O^+} remains to be estimated.

Tomographic inversion

The inversion domain covers $-40° \le \lambda \le 40°$ in geographic latitude and 100 km ≤ a ≤ 800 km in altitude. As the longitudinal range of the inversion domain is centered around the longitude where each orbit crosses the equator, it depends on the orbit of the ISS. The width of the longitudinal range is fixed at 70°. We represent the spatial distribution of $n_{O^+}^2$ of the inversion domain in the following form:

$$[n_{O^+}(\boldsymbol{r})]^2 = \sum_{i=1}^{N} w_i b(\boldsymbol{r}, \boldsymbol{r}_i), \tag{6}$$

where w_i is the weight for the basis function $b(\boldsymbol{r}, \boldsymbol{r}_i)$ and N denotes the number of the basis functions used for the estimation. We define the basis function b as

$$b(\boldsymbol{r}, \boldsymbol{r}_i) = B\left(\frac{\lambda - \lambda_i}{\Delta\lambda}\right) B\left(\frac{\varphi - \varphi_i}{\Delta\varphi}\right) B\left(\frac{a - a_i}{\Delta a}\right), \tag{7}$$

where λ, φ, and a indicate the geographic latitude, geographic longitude, and altitude, respectively. The function B denotes the second-order cardinal B-spline function centered at zero (Fahrmeir et al. 2021):

$$B(z) = \begin{cases} \frac{1}{2}\left(z + \frac{3}{2}\right)^2 & \left(-\frac{3}{2} \le z < -\frac{1}{2}\right) \\ \frac{3}{4} - z^2, & \left(-\frac{1}{2} \le z < \frac{1}{2}\right) \\ \frac{1}{2}\left(\frac{3}{2} - z\right)^2 & \left(\frac{1}{2} \le z < \frac{3}{2}\right), \\ 0, & (\text{otherwise}). \end{cases} \tag{8}$$

In Eq. (7), we set $\Delta\lambda = 2°$, $\Delta\varphi = 5°$, and $\Delta a = 20\,\mathrm{km}$. This means that the basis function is placed every 2°, 5°, and 20 km in geographic latitude, longitude, and altitude, respectively.

To ensure that the O^+ density represented by Eq. (6) is positive, we apply the constraint $w_i > 0$ and convert it into a logarithm as

$$x_i = \log w_i. \tag{9}$$

We define a N-dimensional vector $\boldsymbol{x}$ consisting of x_i for all the basis functions and assume that $\boldsymbol{x}$ does not change over time for each orbit. The prediction of the observation (counts per min) for the jth pixel at time t_k can thus be written as a function of $\boldsymbol{x}$:

$$\begin{aligned} h_{kj}(\boldsymbol{x}) &= \frac{s_j}{4\pi}\int \kappa e^{-\tau(\boldsymbol{r})}\left(\sum_i e^{x_i} b(\boldsymbol{r},\boldsymbol{r}_i)\right) d\ell \\ &\quad + \mu = \frac{s_j}{4\pi}\sum_i e^{x_i}\int \kappa e^{-\tau(\boldsymbol{r})} b(\boldsymbol{r},\boldsymbol{r}_i)\, d\ell + \mu, \end{aligned} \tag{10}$$

where μ is a constant accounting for the background incident EUV, which is assumed to be uniform over all the pixels.

We estimate the O^+ distribution based on the Bayesian formulation, as also done by Dymond et al. (2017a). We assume the observed count of EUV photons for each pixel y_{kj} obeys the Poisson distribution as

$$y_{kj} \sim \mathrm{Poisson}\left(\mathrm{h_{kj}}(\boldsymbol{x})\right). \tag{11}$$

Defining a vector $\boldsymbol{y}_k$ consisting of y_{kj} for all the pixels used for the estimation in each image, the likelihood of $\boldsymbol{x}$ given $\boldsymbol{y}_k$ can be written as

$$p(\boldsymbol{y}_k|\boldsymbol{x}) = \prod_{j=1}^{n} \frac{h_{kj}(\boldsymbol{x})^{y_{kj}}}{y_{kj}!}\exp\left[-h_{kj}(\boldsymbol{x})\right], \tag{12}$$

where n is the dimension of $\boldsymbol{y}_k$ which corresponds to the number of the pixels used for the estimation in each image. The prior distribution for $\boldsymbol{x}$ is given by a Gaussian distribution as

$$p(\boldsymbol{x}) = \frac{1}{\sqrt{(2\pi)^N|\mathbf{P}_x|}}\exp\left(-\frac{1}{2}[\boldsymbol{x}-\bar{\boldsymbol{x}}_b]^{\mathsf{T}}\mathbf{P}_x^{-1}[\boldsymbol{x}-\bar{\boldsymbol{x}}_b]\right), \tag{13}$$

where $\bar{\boldsymbol{x}}_b$ is the prior mean, $\mathbf{P}_x$ is the prior covariance matrix, and $|\mathbf{P}_x|$ indicates the determinant of $\mathbf{P}_x$. The prior mean $\bar{\boldsymbol{x}}_b$ is given by the average of the IRI density over the estimation domain for each altitude. The covariance matrix $\mathbf{P}_x$ is obtained from the Gaspari–Cohn covariance function (Gaspari and Cohn 1999):

$$\rho(d) = \begin{cases} 1 - \frac{5}{3}d^2 + \frac{5}{8}d^3 + \frac{1}{2}d^4 - \frac{1}{4}d^5, & (0 \le d < 1) \\ 4 - 5d + \frac{5}{3}d^2 + \frac{5}{8}d^3 - \frac{1}{2}d^4 + \frac{1}{12}d^5 - \frac{2}{3d}, & (1 \le d < 2) \\ 0, & (d \ge 2) \end{cases} \tag{14}$$

which approximates a Gaussian function but provides a sparse covariance matrix. To obtain the covariance between two points $\boldsymbol{r}_1$ and $\boldsymbol{r}_2$, we define d as

$$d(\boldsymbol{r}_1,\boldsymbol{r}_2) = \frac{|\lambda_1^* - \lambda_2^*|^2}{\Delta\lambda^{*2}} + \frac{|\varphi_1 - \varphi_2|^2}{\Delta\varphi^2} + \frac{|a_1 - a_2|^2}{\Delta a^2}, \tag{15}$$

where λ_i^*, φ_i, and a_i denote the geomagnetic dip latitude, geographic longitude, and altitude of the point $\boldsymbol{r}_i$, respectively. Although the spatial scale of the basis function is given in Eq. (7), the effective spatial scale can be controlled by $\Delta\lambda^*$, $\Delta\varphi$, and Δa in Eq. (15) which determines the spatial scale of the covariance function $\rho(d)$. In this study, we set $\Delta\lambda^* = 5°$, $\Delta\varphi = 60°$, and $\Delta a = 50\mathrm{km}$. Note that Eq. (15) uses dip latitudes, which means that we assume high correlation between two points with similar dip latitudes. The covariance matrix $\mathbf{P}_x$ is then obtained as follows:

$$\mathbf{P}_x = \sigma^2 \begin{pmatrix} \rho(d(\boldsymbol{r}_1,\boldsymbol{r}_1)) & \rho(d(\boldsymbol{r}_1,\boldsymbol{r}_2)) & \cdots & \rho(d(\boldsymbol{r}_1,\boldsymbol{r}_N)) \\ \rho(d(\boldsymbol{r}_2,\boldsymbol{r}_1)) & \rho(d(\boldsymbol{r}_2,\boldsymbol{r}_2)) & \cdots & \rho(d(\boldsymbol{r}_2,\boldsymbol{r}_N)) \\ \vdots & \vdots & \ddots & \vdots \\ \rho(d(\boldsymbol{r}_N,\boldsymbol{r}_1)) & \rho(d(\boldsymbol{r}_N,\boldsymbol{r}_2)) & \cdots & \rho(d(\boldsymbol{r}_N,\boldsymbol{r}_N)) \end{pmatrix}, \tag{16}$$

where σ is a parameter which determines the scale of $\mathbf{P}_x$.

The posterior density of $\boldsymbol{x}$ given a sequence of EUV images $\{\boldsymbol{y}_1,\ldots,\boldsymbol{y}_K\}$ acquired in each ISS orbit is written as

$$p(\boldsymbol{x}|\boldsymbol{y}_1,\ldots,\boldsymbol{y}_K) = \frac{p(\boldsymbol{x})\prod_{k=1}^K p(\boldsymbol{y}_k|\boldsymbol{x})}{\int p(\boldsymbol{x})\prod_{k=1}^K p(\boldsymbol{y}_k|\boldsymbol{x})\,d\boldsymbol{x}}. \tag{17}$$

Using Eqs. (12) and (13), we find

$$\begin{aligned} &p(\boldsymbol{x}|\boldsymbol{y}_1,\ldots,\boldsymbol{y}_K) \\ &\propto p(\boldsymbol{x})\prod_{k=1}^K p(\boldsymbol{y}_k|\boldsymbol{x}) \\ &= \frac{1}{\sqrt{(2\pi)^N|\mathbf{P}_x|}}\exp\left(-\frac{1}{2}[\boldsymbol{x}-\bar{\boldsymbol{x}}_b]^{\mathsf{T}}\mathbf{P}_x^{-1}[\boldsymbol{x}-\bar{\boldsymbol{x}}_b]\right) \\ &\quad \prod_{k=1}^K\prod_{j=1}^n \frac{h_{kj}(\boldsymbol{x}_k)^{y_{kj}}}{y_{kj}!}\exp\left[-h_{kj}(\boldsymbol{x}_k)\right]. \end{aligned} \tag{18}$$

Accordingly, the log posterior density satisfies

$$\begin{aligned}\log p(\boldsymbol{x}|\boldsymbol{y}_1,\ldots,\boldsymbol{y}_K) &= -\frac{1}{2}[\boldsymbol{x}-\bar{\boldsymbol{x}}_b]^{\mathsf{T}}\mathbf{P}_x^{-1}[\boldsymbol{x}-\bar{\boldsymbol{x}}_b] \\ &+\sum_{k=1}^{K}\sum_{j=1}^{n}\left[y_{kj}\log h_{kj}(\boldsymbol{x})-\log y_{kj}!-h_{kj}(\boldsymbol{x})\right] \\ &-\frac{1}{2}\log\left[(2\pi)^N|\mathbf{P}_x|\right]+\mathrm{C},\end{aligned} \tag{19}$$

where C is a constant. We define the objective function J as

$$\begin{aligned}J &= \frac{1}{2}[\boldsymbol{x}-\bar{\boldsymbol{x}}_b]^{\mathsf{T}}\mathbf{P}_x^{-1}[\boldsymbol{x}-\bar{\boldsymbol{x}}_b] \\ &-\sum_{k=1}^{K}\sum_{j=1}^{n}\left[y_{kj}\log h_{kj}(\boldsymbol{x})-\log y_{kj}!-h_{kj}(\boldsymbol{x})\right],\end{aligned} \tag{20}$$

and minimize J to obtain the optimal value $\hat{\boldsymbol{x}}$ which maximizes the posterior density $p(\boldsymbol{x}|\boldsymbol{y}_1,\ldots,\boldsymbol{y}_K)$. The minimization of J is conducted with the Newton–Raphson method as explained in Appendix. An estimate of the O^+ density distribution is eventually obtained as

$$n_{O^+}(\boldsymbol{r}) = \sqrt{\sum_i e^{\hat{x}_i}b_i(\boldsymbol{r},\boldsymbol{r}_i)}. \tag{21}$$

The uncertainties of the estimate can be evaluated with the variance of the posterior distribution $p(\boldsymbol{x}|\boldsymbol{y}_1,\ldots,\boldsymbol{y}_K)$, where J is the objective function defined in Eq. (20). The second-order approximation of J yields an approximation of the posterior distribution as follows

$$\begin{aligned}p(\boldsymbol{x}|\boldsymbol{y}_1,\ldots,\boldsymbol{y}_K) \approx\ \exp\Bigg[&-J(\hat{\boldsymbol{x}})-\frac{1}{2}(\boldsymbol{x}-\hat{\boldsymbol{x}})\left[\nabla^2 J\right](\boldsymbol{x}-\hat{\boldsymbol{x}}) \\ &-\frac{1}{2}\log\left[(2\pi)^N|\mathbf{P}_x|\right]+C\Bigg].\end{aligned} \tag{22}$$

This approximation is sometimes referred to as Laplace's approximation (e.g., Bishop 2006) and it provides a Gaussian approximation of the posterior. We can thus regard the inverse of the Hessian matrix $\left(\nabla^2 J\right)^{-1}$ as an approximation of the covariance matrix of the posterior distribution. We evaluate the uncertainties using the diagonal elements of $\left(\nabla^2 J\right)^{-1}$ in this study.

Parameter estimation

To obtain an estimate of the O^+ density with the above method, the parameters μ in Eq. (10) and σ^2 in Eq. (16) must be obtained in advance. We determine these parameters by maximizing the marginal likelihood (e.g., Morris 1983; Casella 1985) of μ and σ^2 defined as

$$\begin{aligned}&p(\boldsymbol{y}_1,\ldots,\boldsymbol{y}_K|\mu,\sigma^2) \\ &= \int p(\boldsymbol{x}|\mu,\sigma^2) \\ &\quad\prod_{k=1}^{K}p(\boldsymbol{y}_k|\boldsymbol{x},\mu,\sigma^2)\,d\boldsymbol{x} \\ &= \int \frac{1}{\sqrt{(2\pi)^N|\mathbf{P}_x|}} \\ &\quad\exp\left(-\frac{1}{2}[\boldsymbol{x}-\bar{\boldsymbol{x}}_b]^{\mathsf{T}}\mathbf{P}_x^{-1}[\boldsymbol{x}-\bar{\boldsymbol{x}}_b]\right) \\ &\quad\prod_{k=1}^{K}\prod_{j=1}^{n}\frac{h_{kj}(\boldsymbol{x}_k)^{y_{kj}}}{y_{kj}!} \\ &\quad\exp\left[-h_{kj}(\boldsymbol{x}_k)\right]d\boldsymbol{x} \\ &= \frac{1}{\sqrt{(2\pi)^N|\mathbf{P}_x|}}\int\exp\left[-J\right]d\boldsymbol{x},\end{aligned} \tag{23}$$

where J is the objective function defined in Eq. (20). The second-order approximation of J in Eq. (22) yields an approximation of Eq. (23) as follows

$$\begin{aligned}p(\boldsymbol{y}_1,\ldots,\boldsymbol{y}_K|\mu,\sigma^2) &\approx \frac{1}{\sqrt{(2\pi)^N|\mathbf{P}_x|}}\frac{\sqrt{(2\pi)^N}\exp[-J(\hat{\boldsymbol{x}})]}{\sqrt{|\nabla^2 J(\hat{\boldsymbol{x}})|}} \\ &= \frac{\exp[-J(\hat{\boldsymbol{x}})]}{\sqrt{|\mathbf{P}_x||\nabla^2 J(\hat{\boldsymbol{x}})|}},\end{aligned} \tag{24}$$

where $|\nabla^2 J(\hat{\boldsymbol{x}})|$ is the determinant of the Hessian matrix of J. The logarithm of the marginal likelihood can thus approximately be obtained as

$$\log p(\boldsymbol{y}_1,\ldots,\boldsymbol{y}_K|\mu,\sigma^2) \approx -J(\hat{\boldsymbol{x}})-\frac{1}{2}\Big(\log|\mathbf{P}_x|+\log|\nabla^2 J(\hat{\boldsymbol{x}})|\Big). \tag{25}$$

We thus seek the optimal values of μ and σ^2 such that $\log p(\boldsymbol{y}_1,\ldots,\boldsymbol{y}_K|\mu,\sigma^2)$ is maximized.

Experiment with synthetic images

We conducted an experiment of reconstructing the O^+ density distribution from a sequence of synthetic images. The synthetic images were generated by simulating the actual observation by the EUVI-B imager at 21:03–21:26 UT on 26 December 2012, and these synthetic images were used as the observation $\{\boldsymbol{y}_1,\ldots,\boldsymbol{y}_K\}$ in Eq. (18). Figure 4 shows the positions of the ISS at the midpoint of each observation interval on 26 December 2012. For the orbit of 21:03–21:26 UT, the imager started observations about 32° latitude and −17° longitude and took 14 images until the observation ended at about −33° latitude and 38° longitude. The imagers were oriented toward the aft direction of the ISS orbit as described above. EUVI-B thus observed EUV which came from the northwest. The O^+ distribution was determined by the IRI model (Bilitza

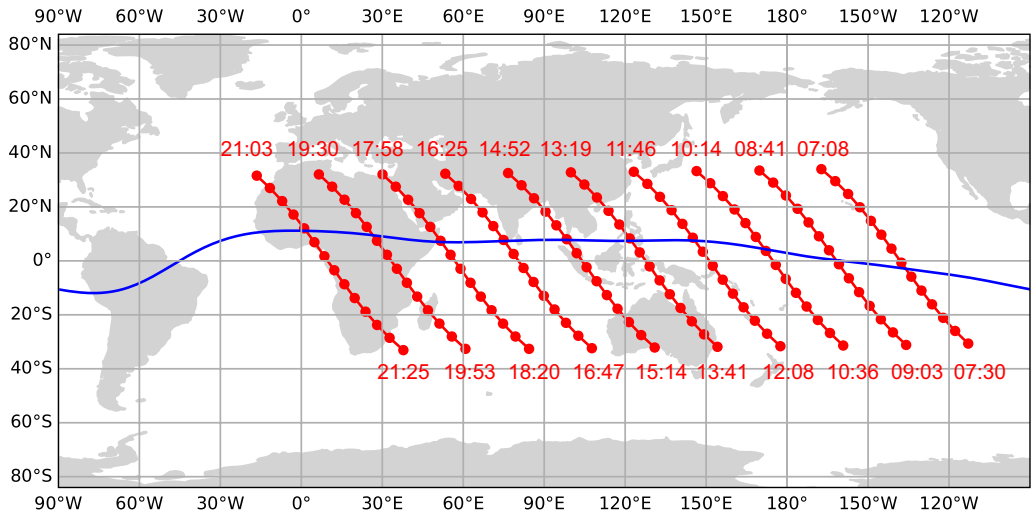

Fig. 4 ISS orbits of 07:08–07:30 UT, 08:41–09:03 UT, 10:14–10:36 UT, 11:46–12:08 UT, 13:19–13:41 UT, 14:52–15:14 UT, 16:25–16:47 UT, 17:58–18:20 UT, 19:30–19:53 UT, and 21:03–21:25 UT on 26 December 2012. The blue line indicates the dip equator according to the DGRF model. Each red circle indicates the location of the ISS at the midpoint of each observation interval (exposure time)

et al. 2014) for obtaining the synthetic images. The observation for each pixel was predicted according to Eq. (10) with the background noise of $\mu = 0.6$, and Poisson noise was added to each pixel of the synthetic images. Figure 5 shows 4 of the 14 synthetic images taken at about 21:08, 21:11, 21:15, and 21:18 UT.

First, we determined the value of the parameters σ and μ with grid search using the metric introduced in Eq. (25). Figure 6 shows the logarithm of the marginal likelihood with respect to the parameter of the background noise μ. The log likelihood reached the maximum when $\mu = 0.6$, which matched the value given for generating synthetic images. This suggests that the log marginal likelihood provides a reasonable estimate of μ. Similarly, we sought the optimal value of σ and it was estimated as 0.8 in this experiment.

We then reconstruct the O^+ distribution from the synthetic dataset using the optimal parameter values. Figure 7 shows the result of the reconstruction. The upper panel shows the reconstructed O^+ distribution, the middle panel shows the O^+ distribution in the IRI model, used for generating the synthetic data, and the lower panel shows the difference between the reconstructed distribution and the IRI distribution. Each panel shows the distribution on a vertical cross-section approximately along the ISS orbit; that is, $-30°$ and $30°$ latitudes correspond to $38°$ and $-33°$ longitudes, respectively. The double-peak structure of the EIA given by the IRI model was successfully reproduced. Note that the color scale is logarithmic in the upper and middle panels while it is linear in the bottom panel. The smaller range in the bottom panel suggests that the reconstructed density distribution matches well with the IRI model which produced the synthetic data. In particular, the errors were small for an altitude of around 300 km, which corresponds to the tangential point of the line of sight for the central pixel. The blue region in the bottom panel indicates underestimation of the O^+ density. The underestimation at around 500 km altitude between $-20°$ and $20°$ latitude was due to this region being out of the scope of the EUVI-B imager.

To assess the area where the O^+ density is effectively estimated from the EUVI-B images, we evaluate the structure of the function $h_{kj}(\boldsymbol{x})$ in Eq. (10). We consider a vector-valued function $\boldsymbol{h}_k(\boldsymbol{x})$ as

$$\boldsymbol{h}_k(\boldsymbol{x}) = \begin{pmatrix} h_{k1}(\boldsymbol{x}) \\ \vdots \\ h_{kn}(\boldsymbol{x}) \end{pmatrix}, \tag{26}$$

and obtain the Jacobian matrix of $\boldsymbol{h}_k(\boldsymbol{x})$ at $\boldsymbol{x} = \boldsymbol{0}$, $\mathbf{H}_k$ as follows

$$\mathbf{H}_k = \begin{pmatrix} (\nabla h_{k1}(\boldsymbol{0}))^\mathsf{T} \\ \vdots \\ (\nabla h_{kn}(\boldsymbol{0}))^\mathsf{T} \end{pmatrix}. \tag{27}$$

We then define a matrix $\mathbf{R}_H$ as follows

$$\mathbf{R}_H = \left(\mathbf{H}_k^\mathsf{T}\mathbf{H}_k\right)^- \mathbf{H}_k^\mathsf{T}\mathbf{H}_k, \tag{28}$$

where $\left(\mathbf{H}_k^\mathsf{T}\mathbf{H}_k\right)^-$ denotes the Moore–Penrose generalized inverse of the matrix $\mathbf{H}_k^\mathsf{T}\mathbf{H}_k$. The matrix $\mathbf{R}_H$ is sometimes

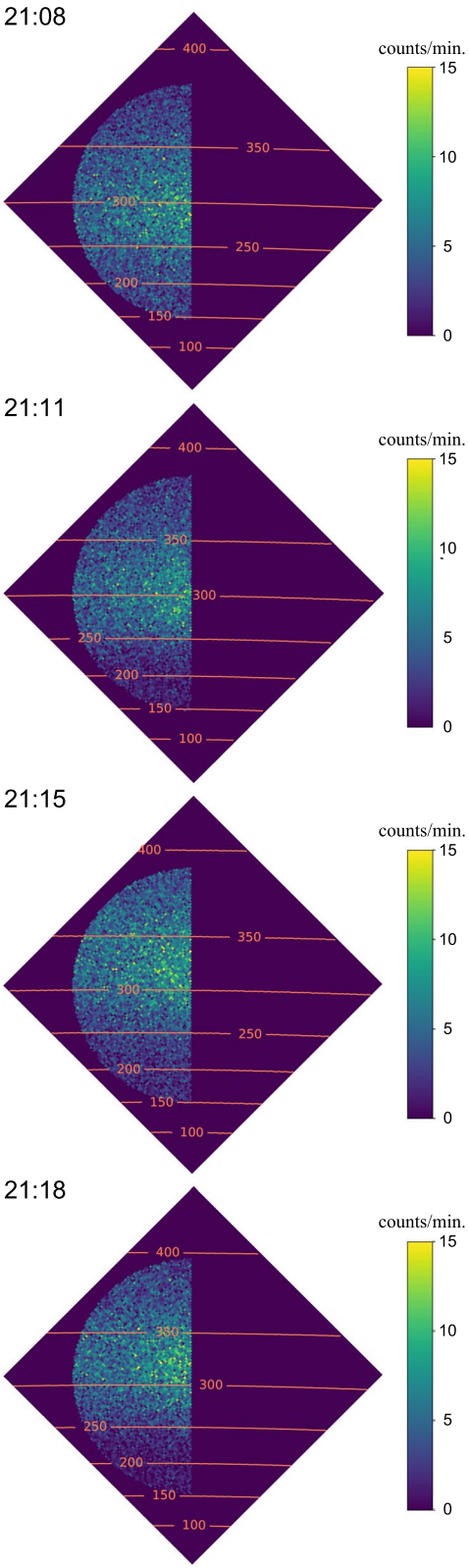

◀ **Fig. 5** The synthetic EUV images which simulate the EUVI-B measurements at about 21:08 UT, 21:11 UT, 21:15 UT, and 21:18 UT. In each panel, the orange contours indicate the altitude at the tangential point of the line of sight for each pixel

referred to as the resolution matrix (e.g., Menke 2018) and it represents how accurately the true weights ($w_1, \cdots$, and w_N in Eq. (6)) can be reproduced. If $\mathbf{R}_H$ is equal to the identity matrix and its diagonal element is unity, the true value can completely be reconstructed by this inversion. The diagonal element is actually less than 1 because the distribution reconstructed by the inversion is blurred from the true distribution. However, if the diagonal element is much smaller than 1, it means that the EUVI-B images are not informative to estimate the O^+ density there. The upper panel of Figure 8 shows the diagonal element of $\mathbf{R}_H$ for each point. The diagonal element was less than 0.2 above 450 km altitudes and below 200 km altitudes. This suggests that the O^+ density above 450 km altitudes and below 200 km altitudes could not reliably be estimated from the EUVI-B images. In the following, we exclude the results in the region where the diagonal element of $\mathbf{R}_H$ is less than 0.2. Accordingly, the region above 450 km altitudes and below 200 km are not displayed in the following analyses. The middle and lower panels of Figure 8 respectively show the O^+ density distribution reconstructed from synthetic images and the difference between the reconstructed distribution and the IRI distribution, which was shown in the top and bottom panels of Figure 7, but the values in the region where the diagonal element of $\mathbf{R}_H$ was below 0.2 are masked. After excluding the estimates with low reliability, the O^+ density was well-estimated and the difference between the reconstructed distribution and the IRI distribution became mostly small. However, the region of the underestimation at around 200–250 km altitudes around 20°–30° latitude was not excluded even after the evaluation of $\mathbf{R}_H$. Figure 9 compares the expected EUV counts under the O^+ distribution from the synthetic images with the expected counts under the IRI O^+ distribution which generated the synthetic images shown in Figure 5. The altitude at the tangential point of the line of sight for each pixel is indicated with orange contours. Each panel of Figure 9a, which shows the expectation under the estimated O^+ distribution, well agreed with the corresponding panel of Figure 9b even for the pixels of which the tangential point was below 250 km. This suggests that the estimates reasonably exploited the information of the EUV images. Since the EUV emissions from the low-altitude region are observed only from distant locations on the orbit of the

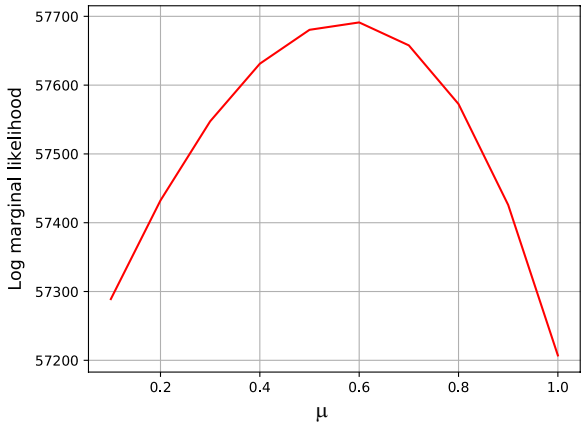

Fig. 6 Logarithm of the marginal likelihood with respect to the parameter of the background noise μ

ISS, it would be difficult to distinguish them from emissions from nearby regions. This is a probable reason of the underestimation at around 200–250 km altitudes in the northern hemisphere.

Figure 10 shows the uncertainties of the estimated O^+ density evaluated with the dispersion of the posterior distribution $p(\boldsymbol{x}|\boldsymbol{y}_1, \ldots, \boldsymbol{y}_K)$. This figure focuses on the altitudinal range from 200 to 450 km. The upper panel shows the estimated O^+ density for reference. The middle panel shows the interquartile range of the posterior distribution of the O^+ density, which can be calculated from the posterior of $x_i = \log w_i$ in Eq. (9) for all i. Since x_i substantially corresponds to the logarithm of the O^+ density, the variance of the estimated density tends to be smaller in the region where the estimated O^+ density is smaller. On the other hand, the lower panel shows the variance of the posterior distribution of x_i for each point, which corresponds to the posterior variance in the logarithmic scale. This tends to be smaller in the region where

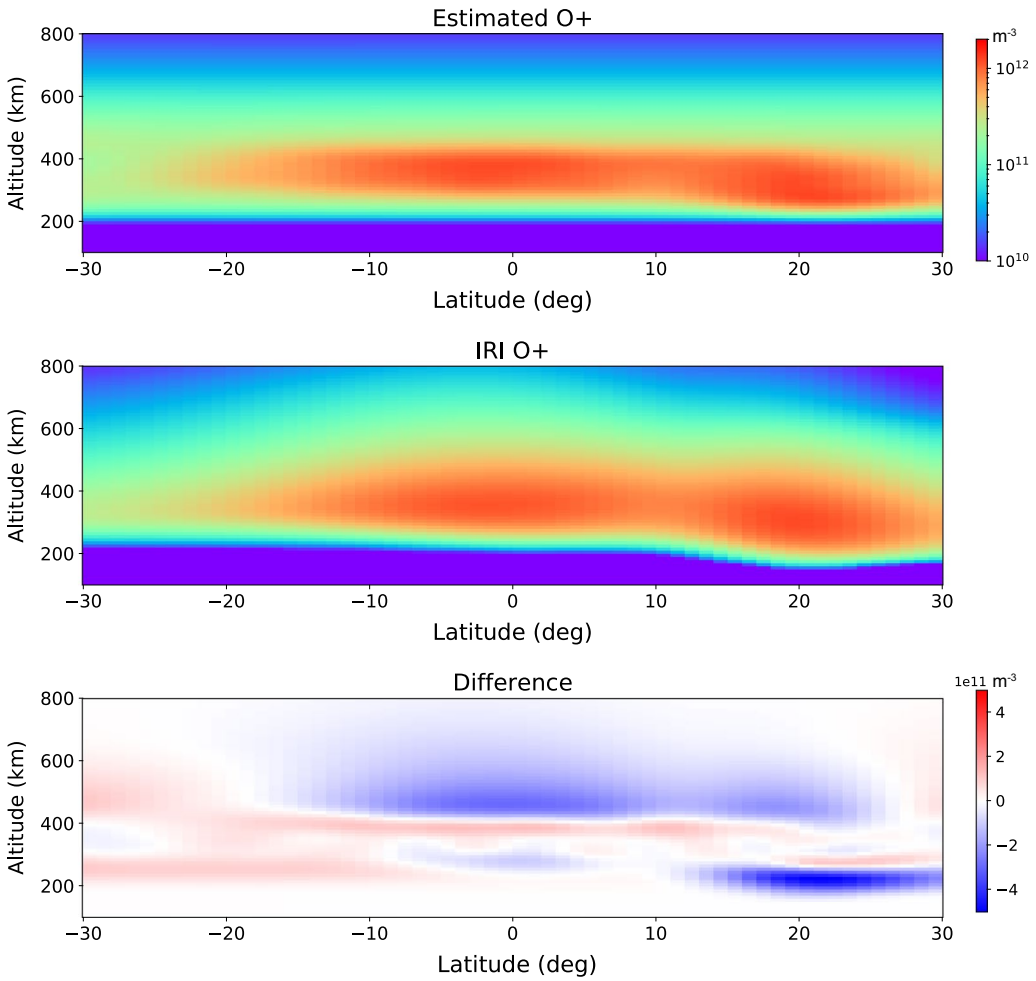

Fig. 7 O^+ distribution estimated from synthetic images (upper), O^+ distribution in the IRI model (middle), and the difference between the two (lower)

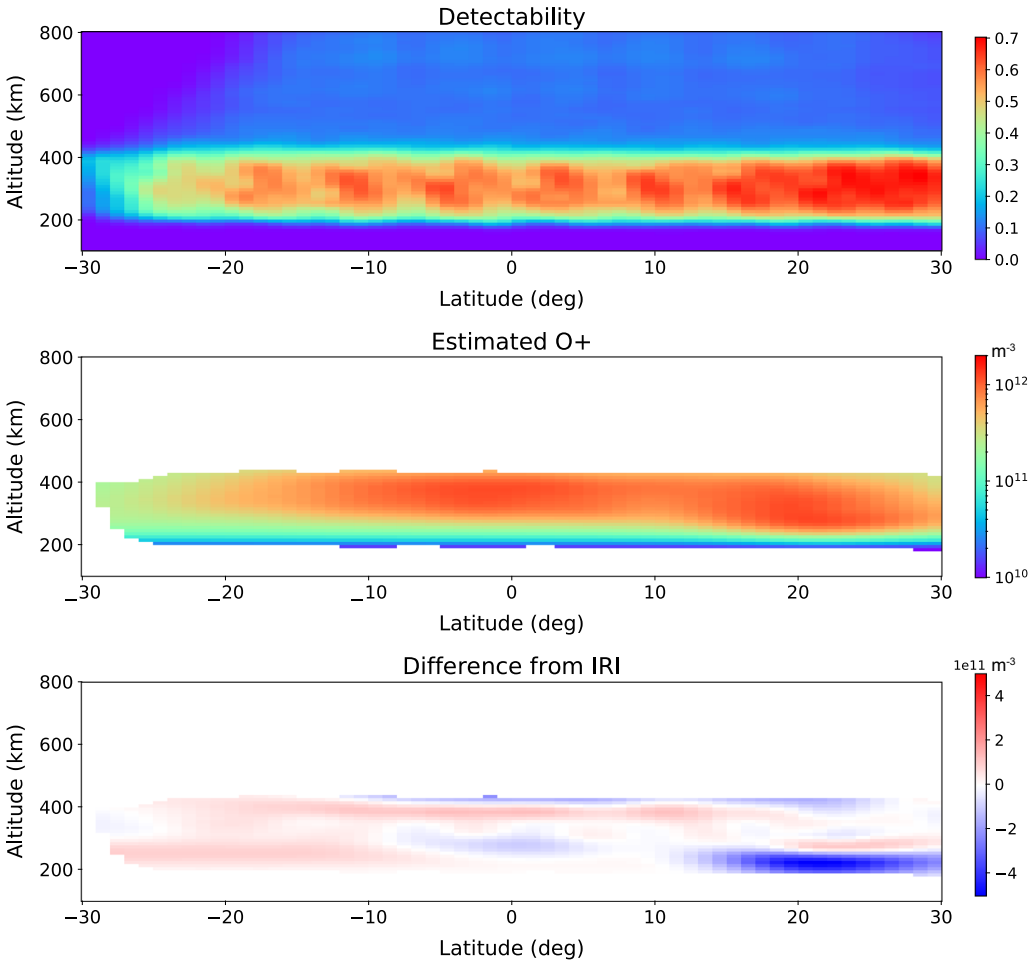

Fig. 8 The diagonal elements of the matrix $\mathbf{R}_H$ (upper), O^+ distribution estimated from synthetic images in the region where the diagonal element is below 0.2 (middle), and the difference between the estimate and the IRI model in the region where the diagonal element is below 0.2 (lower)

the estimated O^+ density is larger. This would be because the observation is related with the line-of-sight integral which corresponds to an additive operation of the O^+ density and the uncertainties tend to be assigned to each w_i along the line-of-sight evenly in linear scale.

Results

This section demonstrates the reconstruction of the O^+ distribution from the actual EUV images for five orbits on 26 December 2012. In estimating the O^+ distribution, the parameters σ and μ were set to be 1.0 and 0.5, respectively, which were determined by the grid search based on the logarithm of the marginal likelihood in Eq. (25). Figures 11 and 12 show the reconstructed O^+ distributions for ten orbits on 26 December 2012 shown in Figure 4. Figure 11 shows the distributions for the orbits in the periods 07:08–07:30 UT, 08:41–09:03 UT, 10:14–10:36 UT, 11:46–12:08 UT, and 13:19–13:41 UT on this day. Figure 12 shows those for the orbits in the periods 14:52–15:14 UT, 16:25–16:47 UT, 17:58–18:20 UT, 19:30–19:53 UT, and 21:03–21:25 UT. On this day, each orbit started around 30° in geographic latitude around 20:30 local time and ended around −30° in geographic latitude around midnight in local time. As shown in Figure 4, the ISS moved from −167° to −113° in geographic longitude during the period 07:08–07:30 UT, from 170° to −136° during 08:41–09:03 UT, from 146° to −159° during 10:14–10:36 UT, from 133° to 178° during 11:46–12:08 UT, from 110° to 154° during 13:19–13:41 UT, from 77° to 131° during 14:52–15:14 UT, from 53° to 108° during 16:25–16:47 UT, from 30° to 84° during 17:58–18:20 UT, from 7° to 61° during 19:30–19:53 UT, and from −17° to 38° during 21:03–21:25 UT. Each panel of Figure 12 shows the O^+ density distribution on the vertical cross-section approximately along the ISS orbit. Figure 13 compares the observed

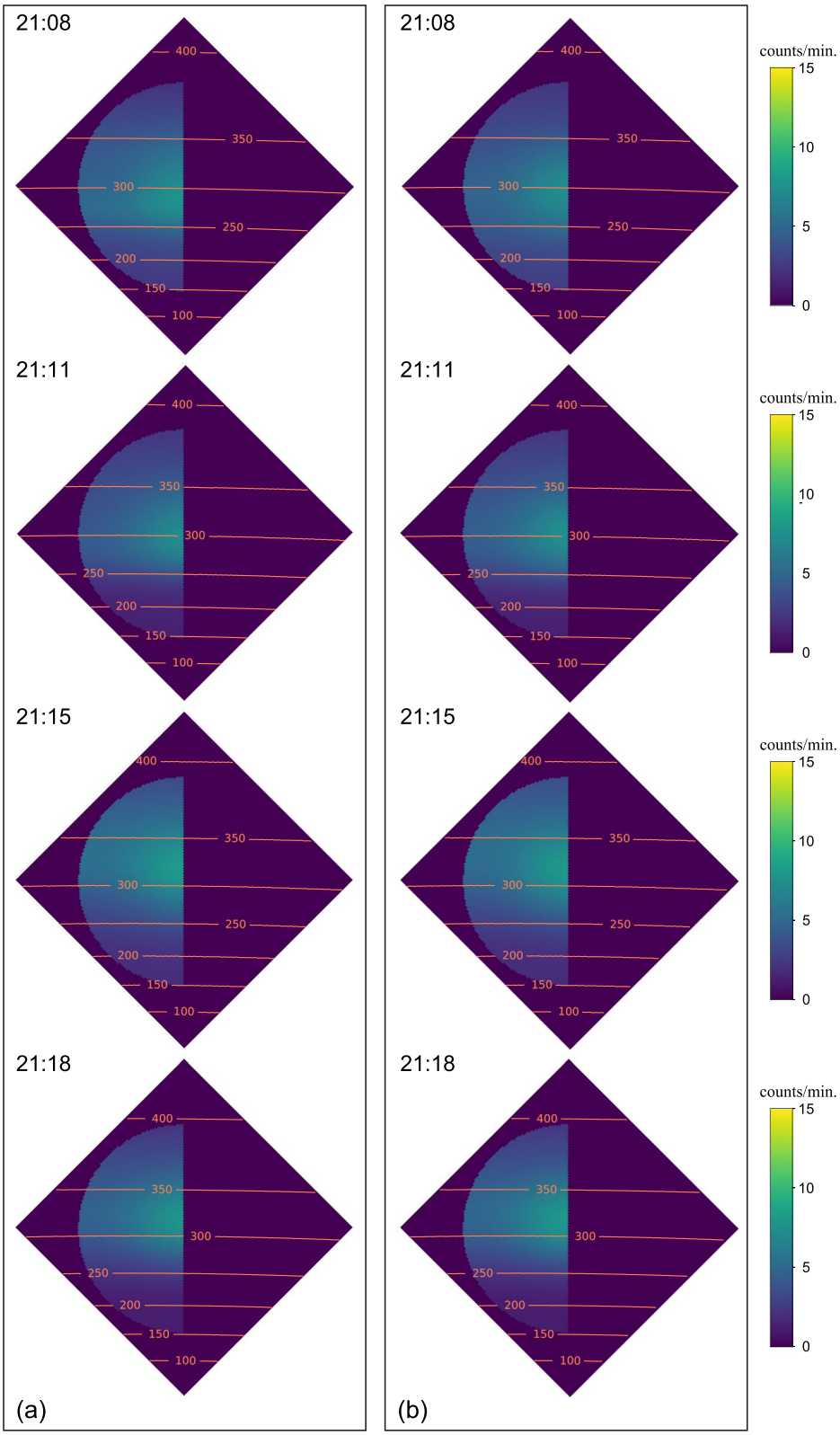

Fig. 9 The expectation of EUV counts under the O^+ distribution estimated from the synthetic images (**a**) and the expectation of EUV counts under the IRI O^+ distribution (**b**) at about 21:08 UT, 21:11 UT, 21:15 UT, and 21:18 UT. The meaning of the orange contours is the same as in **Figure 5**

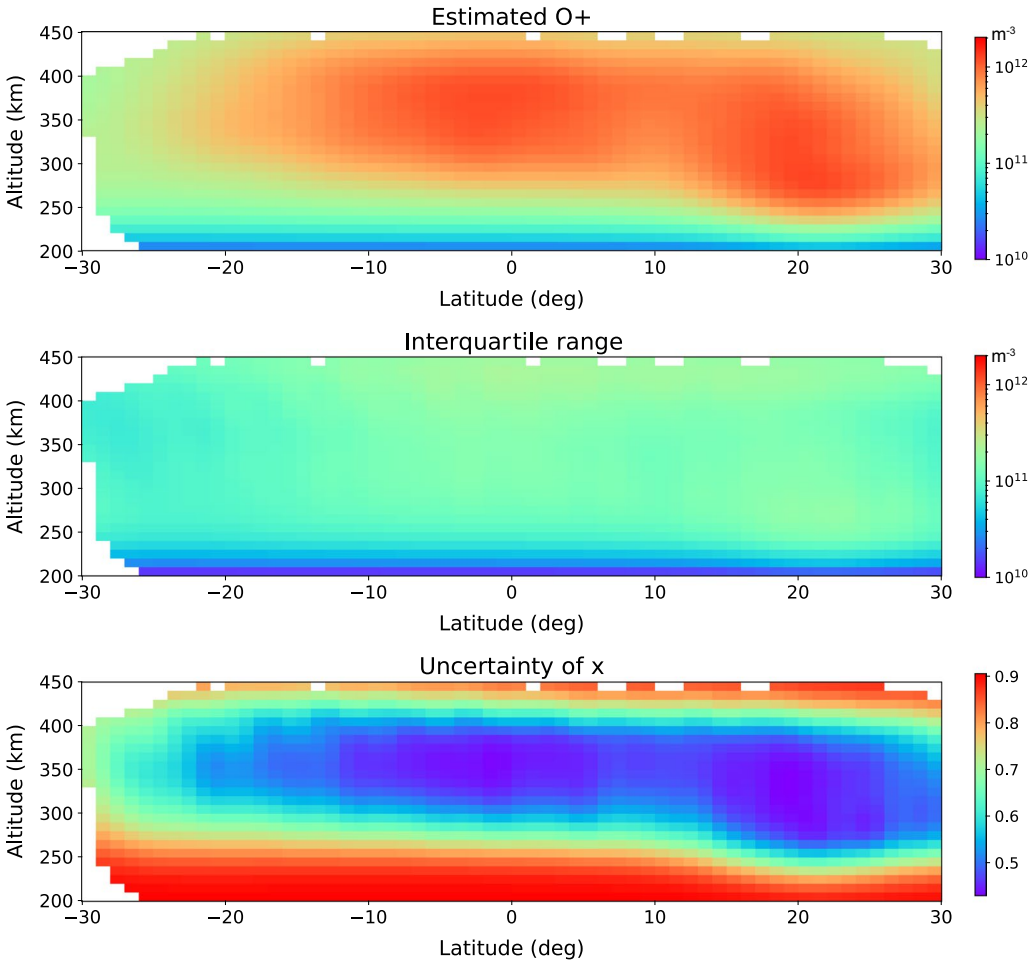

Fig. 10 O^+ distribution estimated from synthetic images (upper), the interquartile range of the posterior distribution of the O^+ density (middle), and the variance of the posterior of $\boldsymbol{x}$ (lower)

EUV images with the expectation of EUV counts under the estimated O^+ distribution at 21:08 UT, 21:11 UT, 21:15 UT, and 21:18 UT. Each panel of Figure 9b well explains the characteristics of the corresponding panel of Figure 9a suggesting that our method provides the reasonable estimates in terms of the EUVI-B data.

Figures 11 and 12 show the clear double-peak structure of the EIA except for the orbit of 14:52–15:14 UT in which the northern peak was not clear. The density tended to be larger in the southern peak than the northern peak. This might be a seasonal effect which enhances the ion density in the summer hemisphere. The structure of the EIA changed orbit by orbit. As mentioned above, the local times were almost the same for each orbit. Hence, the differences between the orbits are interpreted as being due to temporal evolution. One possible cause of the temporal evolution is the longitudinal dependence of the EIA structure. Since the generation of the EIA is related to the dip angle of the background geomagnetic field, the longitudinal variation of the dip angle could cause the variation of the EIA. Indeed, the EIA shifted northward from the period 07:08–07:30 UT to the period 10:14–10:36 UT, which likely corresponds to the location of the dip equator with respect to the orbit. In Figure 4, the dip equator according to the Definitive geomagnetic reference field (DGRF) model (Thébault et al. 2015; Alken et al. 2021) is overplotted. While the orbit at 07:08–07:30 UT crossed the dip equator at around −3° in geographic latitude, the orbit at 10:14–10:36 UT crossed the dip equator at around 4° in geographic latitude. This would explain the latitudinal displacement of the EIA. However, the latitude of the dip equator cannot explain all the characteristics. For example, the separation between the northern and southern anomalies is difficult to explain. At 14:52–15:14 UT, the double-peak structure of the EIA was not observed. At 16:28–16:47 UT, both the

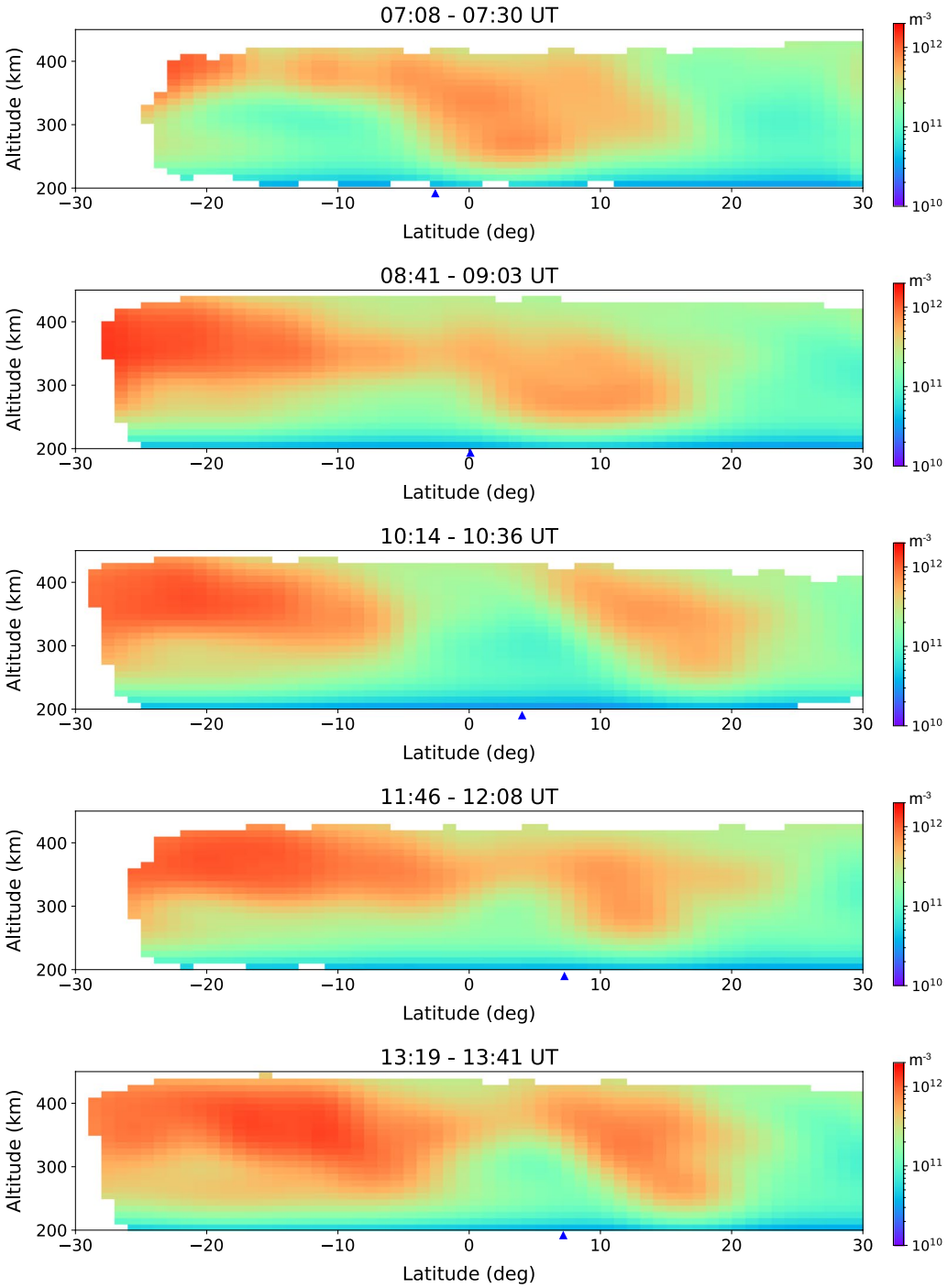

Fig. 11 Reconstructed O^+ distribution for the orbits of 07:08–07:30 UT, 08:41–09:03 UT, 10:14–10:36 UT, 11:46–12:08 UT, and 13:19–13:41 UT on 26 December 2012. Respective orbits covered the longitudinal range from −167° to−113°, from 170° to −136°, from 146° to −159°, from 133° to 178°, and from 110° to 154°. The dip equator for each orbit is indicated with a blue triangle under each panel

northern and southern density anomalies appeared but they were not clearly separated. At 17:58–18:20 UT and 19:32–19:53 UT, the northern anomaly gradually shifted northward and separated from the southern anomaly. At 21:05–21:26 UT, the northern anomaly was distinctly separated from the southern anomaly. The geographic latitude of the dip equator was almost constant around 7° over the longitudes 40° to 140°. The latitudes of the

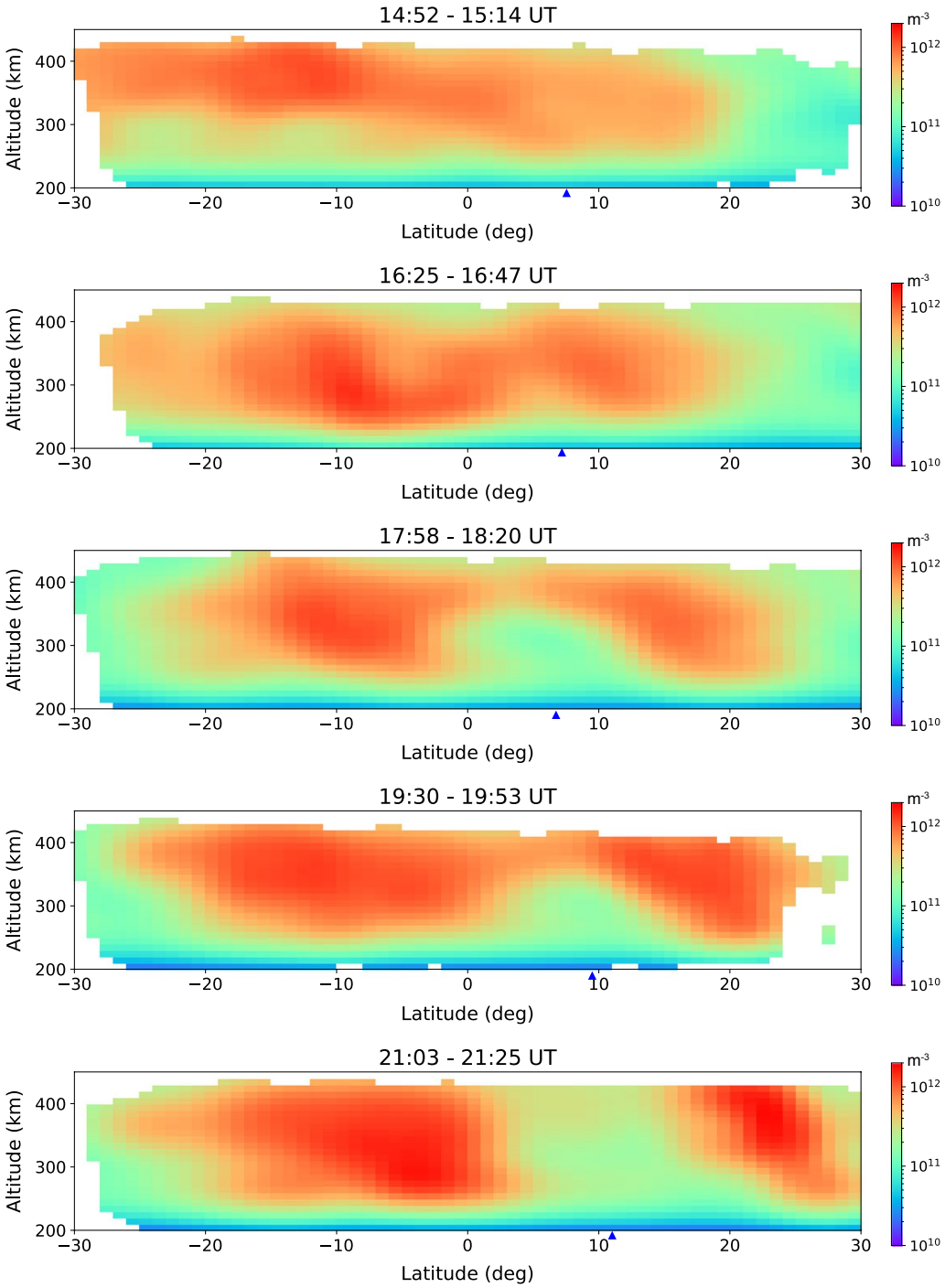

Fig. 12 Reconstructed O^+ distribution for the orbits of 14:52–15:14 UT, 16:25–16:47 UT, 17:58–18:20 UT, 19:30–19:53 UT, and 21:03–21:25 UT on 26 December 2012. Respective orbits covered the longitudinal range from 77° to 131°, from 53° to 108°, from 30° to 84°, from 7° to 61°, and from −17° to 38°. The dip equator for each orbit is indicated with a blue triangle under each panel

dip equator are not likely to explain the variation from the 14:52–15:14 UT orbit to of 19:30–19:53 UT orbit. It is also notable that the peak O^+ density was markedly larger at 21:05–21:26 UT than in the other periods. This density enhancement cannot be explained by the effect of the terrestrial magnetic structure. Although we have not yet resolved the reasons for these characteristics, the density enhancement could be interpreted as the effect

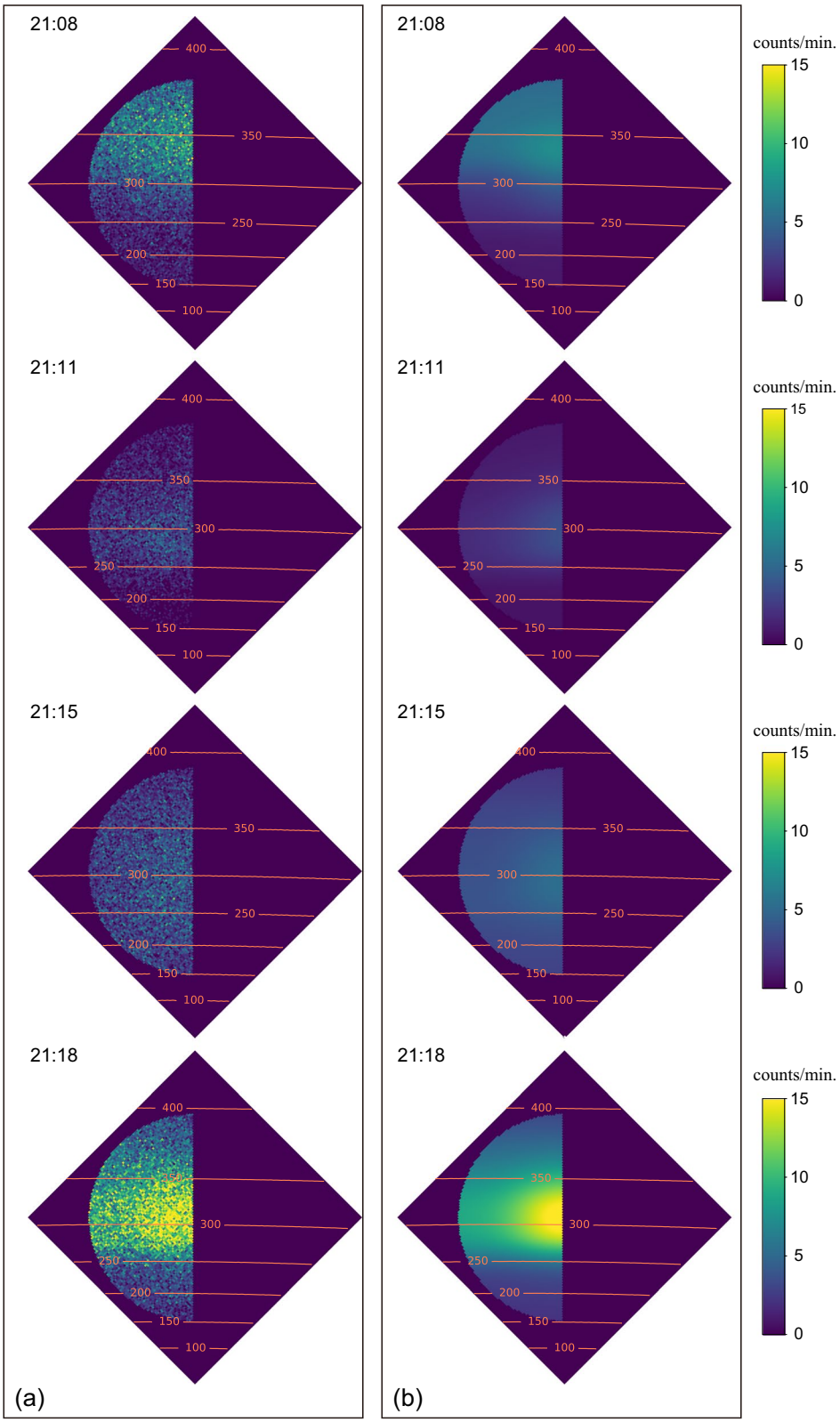

Fig. 13 The observed EUV images (**a**) and the expectation of EUV counts under the estimated O^+ distribution (**b**) at 21:08 UT, 21:11 UT, 21:15 UT, and 21:18 UT. The meaning of the orange contours is the same as in **Figure 5**

of the daytime electric field enhancement (e.g., Mo et al., 2018; Kumar et al., 2021). Indeed, a weak ionospheric convection enhancement driven by the southward interplanetary magnetic field was observed in the *AU* and *AL* indices (Davis and Sugiura , 1966; World Data Center for Geomagnetism, Kyoto et al. 2015) around 12 and 13 UT when the African region was on the dayside, and this region was passed through by the ISS at 19:30–19:53 UT and 21:05–21:26 UT. In addition, wave-4 structures as an effect from the lower atmosphere (e.g., Immel et al., 2006) might also partly contribute to the variations of the EIA. Further analyses are required to clarify what controlled the variation of the EIA.

Summary

We have demonstrated that the O^+ density distribution in the nightside ionosphere can be reconstructed from a sequence of images taken by the EUVI-B imager of ISS-IMAP. Our reconstruction method is based on the representation of the square of the O^+ density using the second-order B-spline functions. The weights of the basis functions are optimized by maximizing the Bayesian posterior density. An estimate of the O^+ distribution can be obtained each orbital period of ISS, approximately every 90 min. An experimental result with a sequence of synthetic images shows that a reasonable estimate for the O^+ distribution is obtained from the EUVI-B data. We presented the density distribution for ten orbits on 26 December 2012 reconstructed from the actual EUVI-B data. The reconstruction results suggest that the structure of the EIA varies orbit by orbit. For example, the results show a latitudinal displacement of the EIA, which was likely to be due to the longitudinal dependence of the background terrestrial magnetic field. A density variation, possibly driven by the daytime electric field, was also observed. In this way, the EUVI-B data can provide vital information for investigating the dynamics of the EIA.

Although we estimated the three-dimensional O^+ distribution, only the latitudinal and altitudinal distribution are demonstrated in the present paper. We assumed a smooth longitudinal structure by setting $\Delta\varphi = 60°$ in Eq. (15) because any clear longitudinal structures were not found in the EUV images analyzed in this study. Due to this assumption, the longitudinal density distribution was hardly resolved. Although it might be possible to resolve a longitudinal structure by tuning $\Delta\varphi$. Note that it is not meaningless to solve the longitudinal distribution in our inversion method. We combine the data of EUV from various directions for estimating the O^+ distribution, and it helps reduce the estimation errors due to measurement noises. To appropriately model the EUV coming from various longitudes, it is necessary to consider the three-dimensional distribution including the longitudinal distribution. The altitudinal resolution is another issue which should be addressed in the future. Although we set $\Delta a = 50$km at present, a higher altitudinal resolution might be feasible by exploiting the resolution of the EUVI-B observation.

Appendix A: Estimation of sensitivity

When estimating the sensitivity at each pixel, we assume that the signal at each pixel can be described by the the following equation:

$$y_j = \bar{\mu} + s_j f_j + \varepsilon_j, \tag{A1}$$

where f_j denotes the incidental EUV flux at each pixel and ε denotes the Poisson noise with zero mean. We assume that f_j obeys the same probability distribution for all the pixels along the red diagonal line in Figure 2. If the mean background noise $\bar{\mu}$ and the sensitivity s_j for each pixel are constant in time, the temporal average of the observed signal $\bar{y}_j$ is given as

$$\bar{y}_j = \bar{\mu} + s_j \bar{f}. \tag{A2}$$

The variance of y_j, σ_{y_j}, becomes

$$\begin{aligned} \sigma_{y_j}^2 &= E\left[s_j^2 (f_j - \bar{f})^2 + \varepsilon_j^2\right] = s_j^2 \sigma_f^2 + E\left[\varepsilon_j^2\right] \\ &= s_j^2 \sigma_f^2 + \bar{y}_j, \end{aligned} \tag{A3}$$

where $E[\cdot]$ denotes the expectation and σ_f is the variance of f. We assumed that the Poisson noise ε_j is independent of f_j and we approximated the variance of ε_j is equal to $\bar{y}_j$. Accordingly, the sensitivity s_j is estimated as follows

$$s_j = \sqrt{\frac{\sigma_{y_j}^2 - \bar{y}_j}{\sigma_f^2}} \propto \sqrt{\sigma_{y_j}^2 - \bar{y}_j}. \tag{A4}$$

Appendix B: Optimization of the objective function

We minimized the objective function J in Eq. (20) with the Newton–Raphson method. Before applying the Newton–Raphson method, we factorize the covariance matrix $\mathbf{P}_x$ as

$$\mathbf{P}_x = \mathbf{V}\mathbf{V}^{\mathsf{T}}. \tag{B1}$$

We define a vector $\boldsymbol{\xi}$ as

$$\boldsymbol{\xi} = \mathbf{V}^{-1}\boldsymbol{x}, \tag{B2}$$

and rewrite the objective function in Eq. (20) as

$$J = \frac{1}{2}\left[\boldsymbol{\xi} - \bar{\boldsymbol{\xi}}_b\right]^{\mathsf{T}}\left[\boldsymbol{\xi} - \bar{\boldsymbol{\xi}}_b\right] - \sum_{k=1}^{K}\sum_{j=1}^{n}\left[y_{kj}\log h_{kj}(\mathbf{V}\boldsymbol{\xi}) - \log y_{kj}! - h_{kj}(\mathbf{V}\boldsymbol{\xi})\right] \tag{B3}$$

to improve convergence. In applying the Newton–Raphson method, we need the gradient of J as

$$\nabla_{\boldsymbol{\xi}} J = \left[\boldsymbol{\xi} - \bar{\boldsymbol{\xi}}_b\right] - \sum_{k=1}^{K}\sum_{j=1}^{n}\left(\frac{y_{kj}}{h_{kj}(\boldsymbol{x})} - 1\right)\mathbf{V}^{\mathsf{T}}\nabla h_{kj}. \tag{B4}$$

We approximately obtained the Hessian matrix of J by neglecting the second-order derivative of the function h_{kj} as also done in the Gauss–Newton method:

$$\nabla^2_{\boldsymbol{\xi}} J \approx \mathbf{I} + \sum_{k=1}^{K}\sum_{j=1}^{n}\frac{y_{kj}}{\left[h_{kj}(\boldsymbol{x})\right]^2}\mathbf{V}^{\mathsf{T}}\nabla h_{kj}\nabla h_{kj}^{\mathsf{T}}\mathbf{V}, \tag{B5}$$

where $\mathbf{I}$ is the identity matrix. We regularized this Hessian matrix at each iteration of the Newton–Raphson method. We thus update x according to the following equation

$$\boldsymbol{x} \longleftarrow \boldsymbol{x} - \frac{\alpha\mathbf{V}\nabla_{\boldsymbol{\xi}} J}{\eta^2\mathbf{I} + \nabla^2_{\boldsymbol{\xi}} J}, \tag{B6}$$

where we fixed η to be 0.5 and α was given adaptively at each iteration.

Note that $\nabla^2_{\boldsymbol{\xi}} J$ in Eq. (B5) is the Hessian matrix of J with respect to $\boldsymbol{\xi}$. When evaluating the uncertainties in Eq. (22), we use the approximate Hessian matrix with respect to $\boldsymbol{x}$ which is given as

$$\nabla^2_{\boldsymbol{x}} J \approx \mathbf{P}_x^{-1} + \sum_{k=1}^{K}\sum_{j=1}^{n}\frac{y_{kj}}{\left[h_{kj}(\boldsymbol{x})\right]^2}\left[\nabla h_{kj}(\boldsymbol{x})\right]\left[\nabla h_{kj}(\boldsymbol{x})\right]^{\mathsf{T}}. \tag{B7}$$

Abbreviations

EUV	Extreme ultraviolet
ISS-IMAP	International Space Station Ionosphere, Mesosphere, Atmosphere, and Plasmasphere mapping
ISS	International Space Station
EIA	Equatorial ionization anomaly
NRLMSISE-00	Naval Research Laboratory Mass Spectrometer and Incoherent Scatter Radar Exosphere 2000
UT	Universal time
IRI	International Reference Ionosphere
DGRF	Definitive geomagnetic reference field

Acknowledgements
The numerical computation in this study was carried out on the Supercomputer System for Statistical Science at ISM under the ISM Cooperative Research Program (2022-ISMCRP-2002).

Author contributions
SN, YH, and AS conceived the study. SN developed the numerical inversion technique YH and AS processed the ISS-IMAP/EUVI-B data. IY, AY, KY, and GM developed the ISS-IMAP/EUVI and calibrated the data. All authors read and approved the final manuscript.

Funding
The work of SN was in part supported by JSPS KAKENHI Grant number JP22H03553.

Availability of data and materials
ISS-IMAP/EUVI data are available via e-mail inquiry to Akinori Saito at Kyoto University (saitoua@kugi.kyoto-u.ac.jp). The code of the IRI model is available via https://irimodel.org/. The code for the NRLMSISE-00 model is available at https://map.nrl.navy.mil/map/pub/nrl/NRLMSIS/.

Declarations

Competing interests
The authors declare that they have no competing interests.

Author details
[1]The Institute of Statistical Mathematics, Tachikawa 190-8562, Japan. [2]Center for Data Assimilation Research and Applications, Joint Support Center for Data Science Research, Tachikawa, Japan. [3]Graduate Institute for Advanced Studies, SOKENDAI, Hayama, Japan. [4]National Institute of Information and Communications Technology, Koganei, Japan. [5]Present Address: The Catholic University of America, Washington, DC, USA. [6]NASA Goddard Space Flight Center, Greenbelt, MD, USA. [7]Graduate School of Science, Kyoto University, Kyoto, Japan. [8]Graduate School of Frontier Sciences, The University of Tokyo, Kashiwa, Japan. [9]Institute of Space and Astronautical Science, Japan Aerospace Exploration Agency, Sagamihara, Japan.

Received: 20 April 2023 Accepted: 9 December 2023
Published online: 02 January 2024

References

Alken P, Thébault E, Beggan CD, Amit H, Aubert J, Baerenzung J, Bondar TN, Brown WJ, Califf S, Chambodut A, Chulliat A, Cox GA, Finlay CC, Fournier A, Gillet N, Grayver A, Hammer MD, Holschneider M, Huder L, Hulot G, Jager T, Kloss C, Korte M, Kuang W, Kuvshinov A, Langlais B, Léger J-M, Lesur V, Livermore PW, Lowes FJ, Macmillan S, Magnes W, Mandea M, Marsal S, Matzka J, Metman MC, Minami T, Morschhauser A, Mound JE, Nair M, Nakano S, Olsen N, Pavón-Carrasco FJ, Petrov VG, Ropp G, Rother M, Sabaka TJ, Sanchez S, Saturnino D, Schnepf NR, Shen X, Stolle C, Tangborn A, Tøffner-Clausen L, Toh H, Torta JM, Varner J, Vervelidou F, Vigneron P, Wardinski I, Wicht J, Woods A, Yang Y, Zeren Z, Zhou B (2021) International geomagnetic reference field: the thirteenth generation. Earth Planets Space 73:49. https://doi.org/10.1186/s40623-020-01288-x

Appleton EV (1946) Two anomalies in the ionosphere. Nature 157:691

Bilitza D, Altadill D, Zhang Y, Mertens C, Truhlik V, Richards P, McKinnell L-A, Reinisch B (2014) The international reference ionosphere 2012: a model of international collaboration. J Space Weather Space Clim 4:A07. https://doi.org/10.1051/swsc/2014004

Bishop CM (2006) Pattern recognition and machine learning. Springer, New York

Casella G (1985) An introduction to empirical Bayes data analysis. Am Stat 39:83–87

Davis TN, Sugiura M (1966) Auroral electrojet activity index *AE* and its universal time variations. J Geophys Res 71:785–801

Dymond KF, Budzien SA, Hei MA (2017) Ionospheric-thermospheric UV tomography: 1. Image space reconstruction algorithm. Radio Sci 52:338–356. https://doi.org/10.1002/2015RS005869
Dymond KF, Nicholas AC, Budzien SA, Stephan AW, Coker C, Hei MA, Groves KM (2017) Ionospheric-thermospheric UV tomography: 2. Comparison with incoherent scatter radar measurements. Radio Sci 52:357–366. https://doi.org/10.1002/2015RS005873
Fahrmeir L, Kneib T, Lang S, Marx BD (2021) Regression—models, methods and applications, 2nd edn. Springer-Verlag, Berlin
Gaspari G, Cohn SE (1999) Construction of correlation functions in two and three dimensions. Q J R Meteorol Soc 125:723–757
Immel TJ, Sagawa E, England SL, Henderson SB, Hagan ME, Mende SB, Frey HU, Swenson CM, Paxton LJ (2006) Control of equatorial ionospheric morphology by atmospheric tides. Geophys Res Lett 33:L15 108. https://doi.org/10.1029/2006GL026161
Kumar A, Chakrabarty D, Pandey K, Fejer BG, Sunda S, Seemala GK, Sripathi S, Yadav AK (2021) Evidence for the significant differences in response times of equatorial ionization anomaly crest corresponding to plasma fountains during daytime and post-sunset hours. J Geophys Res 126:e2020JA028628. https://doi.org/10.1029/2020JA028628
Meléndez-Alvira DJ, Meier RR, Picone JM, Feldman PD, McLaughlin BM (1999) Analysis of the oxygen nightglow measured by the Hopkins Ultraviolet Telescope: implications for ionospheric partial radiative recombination rate coefficients. J Geophys Res 104:14901–14913
Menke W (2018) Geophysical data analysis: discrete inverse theory, 4th edn. Academic Press Inc, San Diego
Mo XH, Zhang DH, Liu J, Hao YQ, Ye JF, Qin JS, Wei WX, Xiao Z (2018) Morphological characteristics of equatorial ionization anomaly crest over Nanning region. Radio Sci 53:37–47. https://doi.org/10.1002/2017RS006386
Morris CM (1983) Parametric empirical Bayes inference: theory and applications. J Am Stat Assoc 78:47–55
Nakano S, Hozumi Y, Saito A, Yoshikawa I, Yamazaki A, Yoshioka K, Murakami G (2021) EUV signals associated with O^+ ions observed from ISS-IMAP/EUVI in the nightside ionosphere. Earth Planets Space 73:151. https://doi.org/10.1186/s40623-021-01479-0
Picone JM, Hedin AE, Drob DP, Aikin AC (2002) NRLMSISE-00 empirical model of the atmosphere: Statistical comparisons and scientific issues. J Geophys Res 107(A12):1468. https://doi.org/10.1029/2002JA009430
Thébault E, Finlay CC, Beggan CD, Alken P, Aubert J, Barrois O, Bertrand F, Bondar T, Boness A, Brocco L, Canet E, Chambodut A, Chulliat A, Coïsson P, Civet F, Du A, Fournier A, Fratter I, Gillet N, Hamilton B, Hamoudi M, Hulot G, Jager T, Korte M, Kuang W, Lalanne X, Langlais B, Léger J-M, Lesur V, Lowes FJ, Macmillan S, Mandea M, Manoj C, Maus S, Olsen N, Petrov V, Ridley V, Rother M, Sabaka TJ, Saturnino D, Schachtschneider R, Sirol O, Tangborn A, Thomson A, Tøffner-Clausen L, Vigneron P, Wardinski I, Zvereva T (2015) International geomagnetic reference field: the 12th generation. Earth Planets Space 67:79. https://doi.org/10.1186/s40623-015-0228-9
Uji K, Yoshikawa I, Yoshioka K, Murakami G, Yamazaki A (2014) Observations of the Earth;s ionosphere and plasmasphere from International Space Station. Trans JSASS Aerospace Tech Jpn 12:Tn47–Tn50
World Data Center for Geomagnetism, Kyoto, Nosé M, Iyemori T, Sugiura M, Kamei T (2015) Geomagnetic *AE* index, data analysis center for geomagnetism and space magnetism, Graduate School of Science, Kyoto University. https://doi.org/10.17593/15031-54800
Yoshikawa I, Homma T, Sakai K, Murakami G, Yoshioka K, Yamazaki A, Sakanoi T, Saito A (2011) Imaging observation of the Earth's plasmasphere and ionosphere by EUVI of ISS-IMAP on the International Space Station. IEEJ Trans Fundam Mater 131:1006–1010. https://doi.org/10.1541/ieejfms.131.1006

Publisher's Note